Title

The detection of the imprint of filaments on cosmic microwave background lensing

Journal

Nature Astronomy, 2(5)

ISSN

2397-3366

Authors

He, Siyu

Alam, Shadab

Ferraro, Simone

et al.

Publication Date

2018-05-01

DOI

10.1038/s41550-018-0426-z

Peer reviewed

nature astronomy

LETTERS

https://doi.org/10.1038/s41550-018-0426-z

The detection of the imprint of filaments on cosmic microwave background lensing

Siyu He[1,2,3]*, Shadab Alam[4,5], Simone Ferraro[6,7], Yen-Chi Chen[8] and Shirley Ho[1,2,3,6]

Galaxy redshift surveys, such as the 2-Degree-Field Survey (2dF)[1], Sloan Digital Sky Survey (SDSS)[2], 6-Degree-Field Survey (6dF)[3], Galaxy And Mass Assembly survey (GAMA)[4] and VIMOS Public Extragalactic Redshift Survey (VIPERS)[5], have shown that the spatial distribution of matter forms a rich web, known as the cosmic web[6]. Most galaxy survey analyses measure the amplitude of galaxy clustering as a function of scale, ignoring information beyond a small number of summary statistics. Because the matter density field becomes highly non-Gaussian as structure evolves under gravity, we expect other statistical descriptions of the field to provide us with additional information. One way to study the non-Gaussianity is to study filaments, which evolve non-linearly from the initial density fluctuations produced in the primordial Universe. In our study, we report the detection of lensing of the cosmic microwave background (CMB) by filaments, and we apply a null test to confirm our detection. Furthermore, we propose a phenomenological model to interpret the detected signal, and we measure how filaments trace the matter distribution on large scales through filament bias, which we measure to be around 1.5. Our study provides new scope to understand the environmental dependence of galaxy formation. In the future, the joint analysis of lensing and Sunyaev–Zel'dovich observations might reveal the properties of 'missing baryons', the vast majority of the gas that resides in the intergalactic medium, which has so far evaded most observations.

Cross-correlations of CMB lensing with tracers of large-scale structure have been widely studied[7–17]. In our study, we detect the imprint of filaments on CMB lensing by cross-correlating filaments with the CMB lensing convergence (κ) map. We use a filament intensity map derived from the Cosmic Web Reconstruction filament catalogue[18] (publicly available at https://sites.google.com/site/yenchicr/catalogue) from the SDSS[2] Baryon Oscillations Spectroscopic Survey[19] Data Release 12 (DR 12)[20]. The filament finder (see Methods section) partitions the Universe from $z=0.005$ to $z=0.700$ into slices with $\Delta z=0.005$. In our study, we use the filaments from $z=0.450$ to $z=0.700$ that are detected from the CMASS galaxy survey (a galaxy sample from SDSS that targets high redshift). Filaments are found in each redshift bin as the density ridge of the smoothed galaxy density field[21], and the filament uncertainty, which describes the uncertainty of the filament position, is also calculated (see Methods). The filament intensity, illustrated in Supplementary Fig. 1, is defined as

$$I(\hat{n},z)=\frac{1}{\sqrt{2\pi\rho_{\rm f}(\hat{n},z)^2}}\exp\left(-\frac{\|\hat{n}-\widehat{\Pi}_{\rm f}(\hat{n},z)\|^2}{2\rho_{\rm f}(\hat{n},z)^2}\right) \quad (1)$$

where $\hat{n}$ is the angular position, $\widehat{\Pi}_{\rm f}(\hat{n},z)$ is the angular position of the closest point to $\hat{n}$ on the nearest filament and $\rho_{\rm f}(\hat{n},z)$ is the uncertainty of the filament at $\widehat{\Pi}_{\rm f}(\hat{n},z)$. Using the intensity map at each redshift bin, we construct the filament intensity overdensity map via

$$\delta_{\rm f}(\hat{n})=\frac{\int I(\hat{n},z){\rm d}z-\bar{I}}{\bar{I}},\quad \bar{I}=\frac{\int I(\hat{n},z){\rm d}\Omega_{\hat{n}}{\rm d}z}{\int {\rm d}\Omega_{\hat{n}}}, \quad (2)$$

where $\Omega_{\hat{n}}$ is the solid angle at $\hat{n}$.

In this work, we use the CMB lensing convergence map (publicly available at http://pla.esac.esa.int/pla/#cosmology) from the Planck[22] satellite experiment. The Planck mission has reconstructed the lensing potential of the CMB from a foreground-cleaned map synthesized from the Planck 2015 full-mission frequency maps using the SMICA code[23]. The lensing convergence is defined in terms of the lensing potential ϕ as

$$\kappa(\hat{n})=\frac{1}{2}\nabla^2_{\hat{n}}\phi(\hat{n}) \quad (3)$$

We measure the cross angular power spectrum (the angular power spectrum of the cross-correlation) of CMB lensing convergence and filaments $C_l^{\kappa f}$ using standard techniques (see 'Estimator' in Methods section). We compute the error for each power spectrum by jackknife resampling the observed area into 77 equally weighted regions (see Supplementary Section 1 and Supplementary Fig. 2) that comprise the CMASS galaxy survey from where the filaments are detected.

We construct a phenomenological model to describe the cross-correlation of filaments and the CMB lensing convergence field. Instead of modelling the filament profile on small scales[24–26], our model studies how filaments trace matter distribution on large scales through the use of the filament bias. We assume a ΛCDM cosmology with Planck parameters from the 2013 release[27], where $\Omega_{\rm m}=0.315$, $h=0.673$, $\sigma_8=0.829$ and $n_{\rm s}=0.9603$. In a spatially flat Friedmann–Robertson–Walker universe described by general relativity, the convergence field is

$$\kappa(\hat{n})=4\pi G_{\rm N}\overline{\rho}_0\int_0^{\chi_{\rm CMB}}\frac{\chi(\chi_{\rm CMB}-\chi)}{\chi_{\rm CMB}}(1+z)\delta_{\rm m}(\chi,\hat{n}){\rm d}\chi \quad (4)$$

[1]Carnegie Mellon University, 5000 Forbes Avenue, Pittsburgh, PA, USA. [2]McWilliams Center for Cosmology, Carnegie Mellon University, Pittsburgh, PA, USA. [3]Lawrence Berkeley National Laboratory, Berkeley, CA, USA. [4]Institute for Astronomy, University of Edinburgh, Edinburgh, UK. [5]Royal Observatory, Blackford Hill, Edinburgh, UK. [6]Berkeley Center for Cosmological Physics, University of California, Berkeley, CA, USA. [7]Miller Institute for Basic Research in Science, University of California, Berkeley, CA, USA. [8]Department of Statistics, University of Washington, Seattle, WA, USA.
*e-mail: siyuh@andrew.cmu.edu

where χ is the comoving radial distance, z is the redshift observed at radial distance, G_N is Newton's gravitational constant, $\overline{\rho_0}$ is the present-day mean density of the Universe, and χ_{CMB} is the comoving distance to the CMB. On a linear scale, we assume that filaments trace the matter as $\delta_f = b_f \delta_m$, where b_f is defined as the large-scale filament bias.

On a large scale, we expect the filament overdensity δ_f to be related to the matter fluctuations through a linear filament bias b_f:

$$\delta_f(\hat{n}) = \int b_f f(z) \delta_m(\hat{n}, z) \mathrm{d}z \tag{5}$$

where $f(z)$ is the mean redshift distribution of the filament intensity, defined as

$$f(z) = \frac{F(z)}{\int F(z)\mathrm{d}z}, \quad F(z) = \frac{1}{\Delta z} \int I(\hat{n}, z) \mathrm{d}\Omega_{\hat{n}} \tag{6}$$

where $I(\hat{n}, z)$ is the filament intensity defined in equation (1) and Δz is the width of a redshift slice. In cross-correlation, on scales smaller than the typical filament length, using filaments introduces additional smoothing compared with the true matter density. We model the smoothing as follows: the filaments have typical length, and we lose all small-scale information about fluctuations along the filament; therefore, we take the corresponding filament power spectrum to be exponentially suppressed below the filament scale $k_{\parallel} \approx 1/$(filament length) in Fourier space. Similarly, any matter in between filaments is either assigned to a filament or eliminated from the catalogue (in underdense regions). For this reason we also introduce a suppression in power in the direction perpendicular to the filaments, with suppression scale $k_{\perp}$. We use two ways to model $k_{\perp}$. The detailed models are shown later in the paper. Using the Limber approximation[28] and the smoothing scale for small scales, the filament–convergence cross-correlation can be written as

$$C_\ell^{\kappa f} = \frac{3H_0^2 \Omega_{m,0}}{2c^2} \int_{z_1}^{z_2} \mathrm{d}z W(z) f(z) \chi^{-2}(z)(1+z) P_{mf}\left(\frac{\ell}{\chi(z)}, z\right) \tag{7}$$

where $W(z) = \chi(z)\left(1 - \frac{\chi(z)}{\chi_{CMB}}\right)$ is the CMB lensing kernel, ℓ is the angular scale in spherical harmonics and P_{mf} is modelled as

$$P_{mf}(k, z) = \frac{1}{2\pi} \int \mathrm{d}\phi b_f P_{mm}(k, z) e^{-(k\cos(\phi)/k_\perp(z))^2 - (k\sin(\phi)/k_{\parallel}(z))^2} \tag{8}$$

where P_{mm} is the matter power spectrum. Sub- and superscript reference: κ, CMB lensing convergence; f, filament; m, matter. C_ℓ^{xy} is the angular power spectrum as a funtion of angular scale ℓ, where xy means the correlation between variables x and y. We use CAMB (Code for Anisotropies in the Microwave Background) (http://www.camb.info/) to evaluate the theoretical spectrum P_{mm}. The measurement of filament length is shown in Fig. 1. The mean and median length of the filaments increases as a function of redshift owing to the combination of two factors. First, the length of the filaments, acting as the mass bridges between galaxy clusters, will decrease. Second, the number of filaments detected also depends on the number density of galaxies, which, in the CMASS sample, is low and decreases as a function of redshift (see Supplementary Fig. 3). The large difference in the mean and median values of filament length indicates that the distribution of the filament length in each redshift bin is not Gaussian. We plot in the background the 2D histogram of filament length distribution as a function of redshift and filament length.

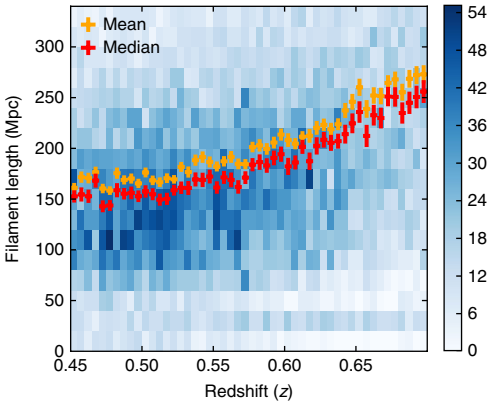

Fig. 1 | The filament length as a function of redshift. The orange (red) crosses are the mean (median) of the filament length in each redshift bin, where the error bars come from the standard error of the mean (median). The large difference in the mean and the median values implies that the filament length distribution is not Gaussian. The background mesh plot shows the 2D histogram of the number of filaments as a function of the redshift and the filament length. The magnitude of the histogram is represented by the colour bar on the right.

To check the validity of our model, we also compare the results to simulations. The excellent agreement that we find in simulations provides an important consistency check. The theoretical prediction for $C_\ell^{\kappa f}$ is shown in equation (7). The matter–filament correlation C_ℓ^{mf} is defined as

$$C_\ell^{mf} = \int_{z_1}^{z_2} \mathrm{d}z \frac{H(z)}{c} f(z) \chi^{-2}(z) P_{mf}\left(\frac{\ell}{\chi(z)}, z\right) \tag{9}$$

By taking the parameters that are slowly varying compared with $f^2(z)$, we get

$$C_\ell^{\kappa f} = \frac{3H_0^2 \Omega_{m,0} W(z)(1+z)}{2cH(z)} C_\ell^{mf} \tag{10}$$

For the filament catalogue, the effective redshift, defined as the weighted mean redshift of filament intensity, is 0.56. This approximation is not perfect, leading to a systematic bias in the prediction for $C_\ell^{\kappa f}$. We propose an estimator for this systematic bias in Supplementary Section 2 (ref. [14]). As shown in Supplementary Fig. 4, the systematic bias is less than 5%. Thus, the approximation only causes a negligible bias. In our analysis, we measure C_ℓ^{mf} using ten realizations of mock sky catalogues of dark matter and corresponding filaments (see Method section).

Figure 2a shows the cross angular power spectrum of filaments and the CMB lensing convergence field. We bin our sample into 16 angular scales. Comparing simulation with data, we get χ^2/d.o.f. = 2.38 (where d.o.f. is degrees of freedom) with all 16 data points and χ^2/d.o.f. = 1.16 without the first data point. The deviation of the first data point from the prediction is likely to be due to cosmic variance, given the small sky area ($f_{sky} = 0.065$) covered by the simulations.

We fit the model of equation (7) to the data with the filament bias b_f as the fitting parameter. We use two different smoothing methods to find $k_{\perp}$. The first method is to define the perpendicular smoothing scale as the filament spacing, since any scale smaller than the filament spacing is smoothed out. The filament spacing is approximately the filament length. Thus, filament length is the overall smoothing scale for the effective power spectrum in

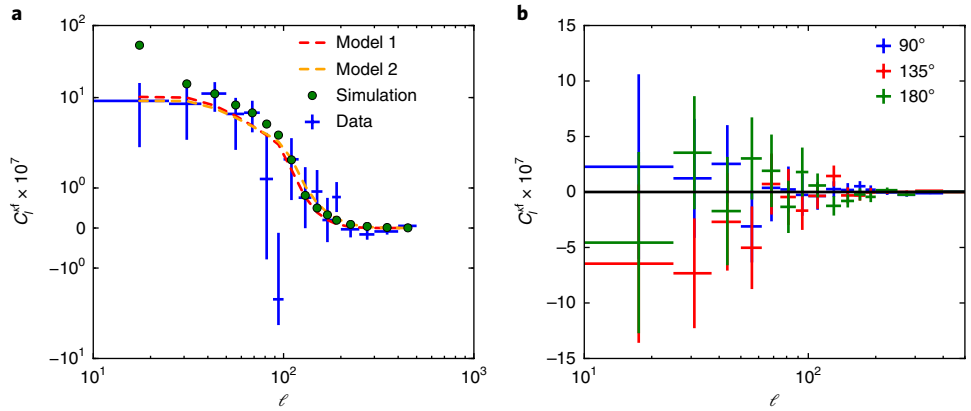

Fig. 2 | Cross angular power spectrum. a, The cross angular power spectrum of the filaments and the CMB convergence field. The blue crosses are measured values, with error bars derived from jackknife resampling of the sky into 77 equally weighted regions. The red and orange dashed lines are theoretical predictions based on different smoothing models (red: filament length used as the smoothing scale both along and perpendicular to the filaments; orange: filament length used as the smoothing scale parallel to filaments, but smoothing scale in the perpendicular direction is fitted as a free parameter). The corresponding filament bias for the two models is 1.68 and 1.47 respectively. The green circles are from simulations. **b**, A null test showing the cross angular power spectrum of the filament catalogue and the rotated CMB lensing convergence map. The error bars are measured from the same jackknife resampling of the sky into 77 equally weighted regions. The cross signals fluctuate around 0. The $\chi^2_{\rm null}$/d.o.f. for the three scenarios are all ~1.

equation (8). The result is shown by the red line in Fig. 2. The best χ^2 fit gives $b_{\rm f}=1.68\pm0.334$. Because filaments also have width, filament spacing may be an overestimate of the smoothing perpendicular to filaments. In the second model, we also fit for smoothing scale in the perpendicular direction as a free parameter, where we assume $1/k_\perp(z)\approx\alpha\times1/k_{||}(z)$, and we obtain $\alpha=0.65$ and $b_{\rm f}=1.47\pm0.28$. The result is shown as the orange line in Fig. 2.

We measure the significance of the cross-correlation detection by measuring the signal-to-noise ratio (SNR). Our SNR is defined as follows

$$S/N=\sqrt{\chi^2_{\rm null}-\chi^2_{\rm fit}} \tag{11}$$

with

$$\chi^2_{\rm null}=\sum_{ij} d_i^{\rm T}(C_{ij}^{-1})d_j \tag{12}$$

$$\chi^2_{\rm fit}=\sum_{ij}(d_i-t_i)^{\rm T}(C_{ij}^{-1})(d_i-t_i) \tag{13}$$

where d_i is the cross angular signal in bin i, t_i is the best-fit theoretical prediction for the cross signal in bin i, and C is the covariance matrix estimated from jackknife resampling. The final result is shown in Table 1. The SNR values for both models show a significant detection of the cross-correlation. On large scales, we find that the filaments trace the matter with a filament bias around 1.5, which is smaller than galaxy bias from the same sample.

To validate the detection of our cross power spectrum, we perform a null test as follows. We rotate the CMB lensing convergence map by 90°, 135° and 180°, and then we cross-correlate these rotated CMB convergence maps with the filament intensity map. Figure 2b shows that the cross signal with the rotated maps fluctuates around 0. The values of $\chi^2_{\rm null}$/d.o.f. for the three cross angular power spectra are 0.79, 0.75 and 1.04, which means that the cross-correlation between rotated CMB maps and the filament intensity map is consistent with 0. In addition, to test the impact of lensing generated by the clusters at the intersection of filaments on our signal, we mask out the redMaPPer clusters[29] in the CMB lensing map, finding a difference of less than 4% in the cross angular power spectrum.

Table 1 | The final result for the bias fitting

	Model 1	Model 2
$b_{\rm f}$	1.68 ± 0.334	1.47 ± 0.28
S/N	5.0	5.2
$\chi^2_{\rm fit}$	25.77	24.39
d.o.f.	15	14

Model 1 uses filament length as the overall smoothing scale. In model 2, the smoothing scale parallel to filaments is the filament length; we fit α for the smoothing in the perpendicular direction, where $1/k_\perp(z)\approx\alpha\times1/k_{||}(z)$. We get α to be 0.65 as the best fit. The bias and the error of bias come from χ^2 fitting of the theoretical model to data.

We define the cross-correlation coefficient between the filament and galaxy maps as $\rho=C_\ell^{\rm fg}/\sqrt{C_\ell^{\rm ff}C_\ell^{\rm gg}}$, where $C_\ell^{\rm fg}$ is the cross angular power spectrum of filaments and galaxies, and $C_\ell^{\rm ff}$ and $C_\ell^{\rm gg}$ are the auto angular power spectra of filaments and galaxies. The result is shown in the left panel of Fig. 3a. The signal is highly correlated on large scales, because both galaxies and filaments trace the large-scale structure of the matter. However, the correlation decreases at small scales. Figure 3b shows the cross-correlation of $C_\ell^{\kappa\rm f}$ and $C_\ell^{\kappa\rm g}$, where $C_\ell^{\kappa\rm g}$ is the angular cross power spectrum of the CMB lensing convergence map and the CMASS galaxy catalogue. These two figures show that the maps are not totally correlated with large deviations at small scales. Establishing the amount of extra cosmological information present in the filament field would require a joint analysis with galaxy clustering and lensing measurements; this is left to future work.

In our work, we have detected the effect of filaments lensing on the CMB by correlating filaments intensity map with CMB lensing convergence map. We measured filament bias, which is a quantitative description of how filaments trace the underlying matter, to be around 1.5. We have performed null tests by rotating the CMB lensing map by more than its correlation length, obtaining results consistent with the null hypothesis. By comparing filaments with galaxies (both at the map and power spectrum level), we have shown an imperfect correlation, indicating that there

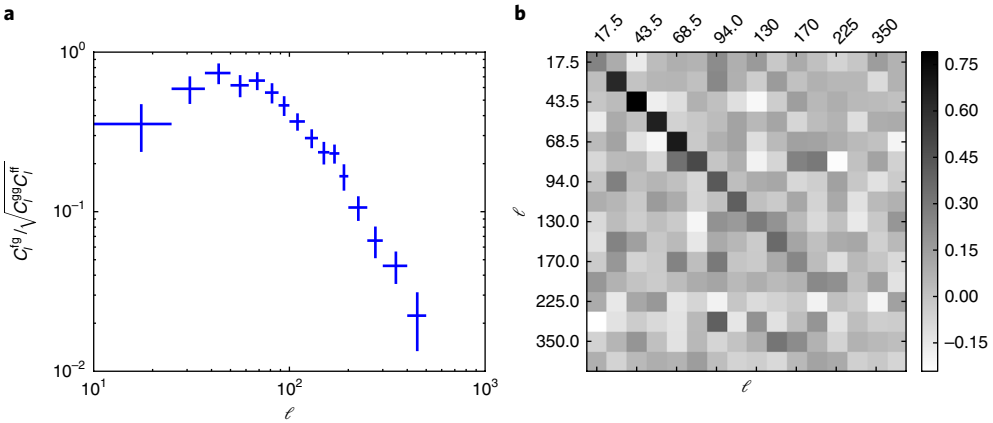

Fig. 3 | Relationship between filament map and galaxy map. a, The correlation coefficient of the galaxy and filament maps, where the error bars are from jackknife resampling of sky into 77 equally weighted regions. **b**, The correlation of $C_\ell^{\kappa\mathrm{f}}$ and $C_\ell^{\kappa\mathrm{g}}$, where the magnitude of correlation is represented in the bar to the right. Both plots show that the filament and galaxy maps are not completely correlated, especially on small scales.

might be additional information in the structure of the cosmic web, of which filaments provide an essential ingredient. In our study, the filament bias measured is significantly different from the mean bias of the CMASS galaxies used to create the filament catalogue. This has important consequences for the environmental dependence of galaxy formation and could be key in generating accurate mocks for the next generations of surveys. In addition, the gas in filaments has been recently detected through the thermal Sunyaev–Zel'dovich effect derived from Planck maps[30] by measuring the gas pressure. A joint analysis of the mass profile and gas pressure could shed light on the majority of the gas in the intergalactic medium that resides outside haloes and has not yet been characterized.

Methods

Filament finder. We obtain filaments from the publicly available Cosmic Web Reconstruction filament catalogue[18]. It finds filaments by applying the ridge detection algorithm (filament detector)[21] to the galaxies in SDSS DR 12, ranging from $z=0.050$ to $z=0.700$. The spectroscopic galaxies are used as they give a reliable redshift estimate. Specifically, the catalogue is constructed using the following steps:

1. Partition the galaxies at redshift $z=0.050$–0.700 into 130 redshift bins such that the bin width is $\Delta z=0.005$. Galaxies within the same bin are projected onto a 2D space.

2. For each bin:

(a) Reconstruct the (2D) galaxy probability density field by applying a kernel density estimator with smoothing bandwidth chosen by the reference rule in ref. [21].

(b) Compute the root mean square (r.m.s.) of the density field (ρ_{rms}) within the area 150 deg < RA < 200 deg and 5 deg < dec. < 30 deg.

(c) Remove galaxies in the regions where the probability density field is below a threshold density.

(d) Apply the ridge detection algorithm[21] to the remaining galaxies.

(e) Apply the galaxy mask to remove filaments outside the region of observations.

Here are some remarks on the construction of the catalogue.

The 2D projection. The Universe is sliced and galaxies are projected onto 2D space for several reasons. First, this enhances the stability of the filament detector. Second, this avoids the problem of the 'finger of god' effect (that is, the galaxy distribution is elongated toward the observer). Third, it is easy to compare filaments across different redshifts. More detailed discussion can be found elsewhere[18].

Choice of Δz. The choice of $\Delta z=0.005$ is to balance the estimation bias and the estimation random error. This is related to the 'bias–variance tradeoff' in statistics[31]. If Δz is small, there will be a limited number of galaxies, so the filament detector will be unstable. On the other hand, if Δz is large, the bin contains a very wide range of the Universe so the filamentary structures may be washed away when projected onto 2D angular space. $\Delta z=0.005$ is an empirical rule that we discovered to apply to the SDSS data.

Area selection for calculating ρ_{rms}. The specific angular space ([150,200] × [5,30] deg^2) is selected to compute the r.m.s. of the density field. The region is chosen because it is a wide region that is almost completely observed in SDSS samples. The range is large enough that the r.m.s. calculation is stable.

Thresholding. Before applying the ridge detection algorithm, galaxies are removed in the low density area. This thresholding stabilizes the ridge detection algorithm because the algorithm is very sensitive to density fluctuations in low density area.

The filament catalogue is shown to have strong agreement with the redMaPPer Catalogue, since most clusters in the redMaPPer Catalogue lie at the intersection of the filaments in the Cosmic Web Reconstruction filament catalogue, as predicted by theory. The filament catalogue also has good consistency with the Voronoi model[21]. Furthermore, a study on the effects of filaments on nearby galaxy properties (stellar mass, brightness, age and orientation) has shown there is strong correlation of galaxy properties with filament environment, which satisfies theoretical predictions[32].

Uncertainty of filaments. The uncertainty of filaments is computed using the bootstrap method[21,33]. The filament detector returns a collection of points on filaments, which we call filament points. For a given redshift bin, denote $F_1, \ldots, F_N$ as filament points. The uncertainty of filament points is computed as follows.

1. All galaxies (in one bin) are re-sampled with replacement to generate a new set of galaxies with the same total number of galaxies. This new set of galaxies is called a bootstrap sample.

2. Apply the same filament-finding algorithm to the galaxies in the bootstrap sample. This yields a new set of filaments, which are called the bootstrap filaments.

3. The distance of the filament point to the nearest filament point in the bootstrap filaments is calculated. Denote as $\epsilon_1, \ldots, \epsilon_N$ the distance for each filament point. This distance serves as an error measurement for $F_1, \ldots, F_N$.

4. Repeat the above three steps 1,000 times (1,000: the number of bootstrap replicates). For each filament point, there will be 1,000 error measurements. For instance, the ith filament point has 1,000 error values: $\epsilon_i^{(1)}, \cdots, \epsilon_i^{(1000)}$.

5. Compute the error (uncertainty) of each filament point by the r.m.s. of the 1,000 error measurements. Namely, for the ith filament point, the error is

$$\mathcal{E}_i=\sqrt{\frac{1}{1,000}\sum_{j=1}^{1,000}\left(\epsilon_i^{(j)}\right)^2}.$$

The bootstrap procedure measures the uncertainty due to the randomness of sampling[33].

Filament length measurement. We take the filament intersections from ref. [18] (publicly available at https://sites.google.com/site/yenchicr/catalogue). For each redshift bin, we use the hierarchical clustering method[21] to determine the number of branches at each intersection. The parameters in the hierarchical clustering are chosen to be the same as[21]:

$$r_{\mathrm{in}}=\frac{2\omega}{3},\quad r_{\mathrm{out}}=2r_{\mathrm{in}},\quad r_{\mathrm{sep}}=(r_{\mathrm{in}}+r_{\mathrm{out}})/2 \tag{14}$$

where $\omega=\omega(z)$ is the smoothing bandwidth. At each intersection, we find the nearest point to the intersection point from each branch, and we group the nearest point as the filament point belonging to that filament (see Supplementary Fig. 5). Then we keep finding the nearest point to the newly grouped filament to find the next filament point belonging to that branch. We stop the loop if the distance

between filament points is less than r_{sep} and the distance between a filament point and the other intersection point is larger than $r_{sep}/2$.

Estimator. We construct the filament map using the HEALPix pixelization31 with Nside = 512. The CMB lensing convergence map is given directly by PLANCK using the HEALPix pixelization with Nside = 2,048. We downgrade the resolution of the lensing convergence map to Nside = 512 to cross-correlate with the filament map. The choice of resolution is consistent with the smoothing applied by the filament finder and is large enough to fully resolve the scales relevant to our cross-correlation.

We measure the cross angular power spectrum for the filament catalogue and the CMB lensing convergence field using a pseudo-C_l estimator:

$$\hat{C}_{\ell}^{\kappa \mathrm{f}}=\frac{1}{(2\ell+1)f_{\mathrm{sky}}^{\kappa \mathrm{f}}}\sum_{m=-\ell}^{\ell}(\delta_{\mathrm{f}})_{\ell m}\kappa_{\ell m}^{*} \tag{15}$$

where $f_{\mathrm{sky}}^{\kappa \mathrm{f}}$ is the sky fraction observed by both the filament catalogue and the CMB lensing convergence field, $\kappa_{\ell m}$ is the spherical harmonic transform of the lensing convergence field and $(\delta_{\mathrm{f}})_{\ell m}$ is the spherical harmonic transform of the filament intensity overdensity. The spherical harmonic transform and C_l are computed using HEALPY.

Sky mock for filaments and dark matter. We use *N*-body simulation runs using the TreePM method[34–36]. We use 10 realizations of this simulation based on the ΛCDM model with $\Omega_{\mathrm{m}}=0.292$ and $h=0.69$. Although the parameters of the simulations are slightly different from the Planck cosmological parameters, if we compare the matter power spectrum with the cosmological parameters from the simulations and Planck, the difference is within 2%. Given the current noise in the data, we believe that this small difference is sub-dominant in our paper. These simulations are in a periodic box of side length $1{,}380h^{-1}$ Mpc and $2{,}048^3$ particles. A friend-of-friend halo catalogue is constructed at an effective redshift of $z=0.55$. This is appropriate for our measurement, as the galaxy sample used has effective redshift of 0.57. We use a halo occupation distribution (HOD)[37–42] to relate the observed clustering of galaxies with halos measured in the *N*-body simulation. We have used the HOD model proposed in[43] to populate the halo catalogue with galaxies.

$$\begin{aligned}\langle N_{\mathrm{cen}}\rangle(M)&=\frac{1}{2}\left[1+\mathrm{erf}\left(\frac{\log M-\log M_{\mathrm{min}}}{\sigma_{\log M}}\right)\right]\\ \langle N_{\mathrm{sat}}\rangle(M)&=\langle N_{\mathrm{cen}}\rangle_{M}\left(\frac{M}{M_{\mathrm{sat}}}\right)^{\alpha}\exp\left(\frac{-M_{\mathrm{cut}}}{M}\right)\end{aligned} \tag{16}$$

where $\langle N_{\mathrm{cen}}\rangle(M)$ is the average number of central galaxies for a given halo mass M and $\langle N_{\mathrm{sat}}\rangle(M)$ is the average number of satellite galaxies. We use the HOD parameter set ($M_{\mathrm{min}}=9.319\times10^{13}M_{\odot}/h$, $M_{\mathrm{sat}}=6.729\times10^{13}M_{\odot}/h$, $\sigma_{\log M}=0.2$, $\alpha=1.1$, $M_{\mathrm{cut}}=4.749\times10^{13}M_{\odot}/h$) from ref. [43]. We have populated central galaxies at the centre of our halo. The satellite galaxies are populated with radius (distance from central galaxy) distributed out to r_{200} as per the Navarro–Frenk–White profile; the direction is chosen randomly with a uniform distribution.

The sky mocks of dark matter and galaxy are obtained from the simulation box using the method described in ref. [44]. We use publicly available MAKE SURVEY (https://github.com/mockFactory/make_survey) code to transform a periodic box into the pattern of the survey. The first step of this transformation involves a volume remapping of the periodic box to sky coordinates preserving the structure in the simulation. This is achieved by using the publicly available package BoxRemap (http://mwhite.berkeley.edu/BoxRemap)[45]. The BoxRemap defines an efficient volume-preserving, structure-preserving and one-to-one map to transform a periodic cubic box to non-cubic geometry. The non-cubic box is then translated and rotated to cover certain parts of the sky. We then convert the cartesian coordinate to the observed coordinate, which is right ascension, declination and redshift. We down-sample the galaxies with redshift to match the mock redshift with the redshift distribution observed in the data. See ref. [44] for more details. We then apply the filament detection algorithm to these simulated mocks using the method described in Filament Finder.

Data availability. The data that support the plots within this paper and other findings of this study are available from the corresponding author upon reasonable request.

Received: 6 September 2017; Accepted: 20 February 2018;
Published online: 9 April 2018

References

1. Colless, M. et al. The 2dF galaxy redshift survey: spectra and redshifts. *Mon. Not. R. Astron. Soc.* **328**, 1039–1063 (2001).
2. Eisenstein, D. J. et al. SDSS-III: massive spectroscopic surveys of the distant universe, the Milky Way galaxy, and extra-solar planetary systems. *Astron. J.* **142**, 72 (2011).
3. Jones, H. D. et al. The 6dF galaxy survey: final redshift release (DR3) and southern large-scale structures. *Mon. Not. R. Astron. Soc.* **399**, 683–698 (2009).
4. Liske, J. et al. Galaxy and mass assembly (GAMA): end of survey report and data release 2. *Mon. Not. R. Astron. Soc.* **452**, 2087–2126 (2015).
5. Scodeggio, M. et al. The VIMOS Public Extragalactic Redshift Survey (VIPERS). Full spectroscopic data and auxiliary information release (PDR-2). *Astron. Astrophys.* **609**, A84 (2018).
6. Bond, R. J., Kofman, L. & Pogosyan, D. How filaments are woven into the cosmic web. *Nature* **380**, 603–606 (1996).
7. Smith, K. M., Zahn, O. & Dore, O. Detection of gravitational lensing in the cosmic microwave background. *Phys. Rev. D* **76**, 043510 (2007).
8. Hirata, C. M., Ho, S., Padmanabhan, N., Seljak, U. & Bahcall, N. A. Correlation of CMB with large-scale structure: II. Weak lensing. *Phys. Rev. D* **78**, 043520 (2008).
9. Bleem, L. E. et al. A measurement of the correlation of galaxy surveys with CMB lensing convergence maps from the South Pole Telescope. *Astron. J.* **753**, L9 (2012).
10. Sherwin, B. D. et al. The Atacama Cosmology Telescope: cross-correlation of CMB lensing and quasars. *Phys. Rev. D* **86**, 083006 (2012).
11. Ferraro, S., Sherwin, B. D. & Spergel, D. N. WISE measurement of the integrated Sachs–Wolfe effect. *Phys. Rev. D* **91**, 083533 (2015).
12. Allison, R. et al. The Atacama Cosmology Telescope: measuring radio galaxy bias through cross-correlation with lensing. *Mon. Not. R. Astron. Soc.* **451**, 849–858 (2015).
13. Giannantonio, T. et al. CMB lensing tomography with the DES Science Verification galaxies. *Mon. Not. R. Astron. Soc.* **456**, 3213–3244 (2016).
14. Pullen, A. R., Alam, S., He, S. & Ho, S. Constraining gravity at the largest scales through CMB lensing and galaxy velocities. *Mon. Not. R. Astron. Soc.* **460**, 4098–4108 (2016).
15. Doux, C. et al. First detection of cosmic microwave background lensing and Lyman-α forest bispectrum. *Phys. Rev. D* **94**, 103506 (2016).
16. Singh, S., Mandelbaum, R. & Brownstein, J. R. Cross-correlating Planck CMB lensing with SDSS: lensing–lensing and galaxy–lensing cross-correlations. *Mon. Not. R. Astron. Soc.* **464**, 2120–2138 (2017).
17. Geach, E. G. & Peacock, J. A. Cluster richness-mass calibration with cosmic microwave background lensing. *Nat. Astron.* **1**, 795–799 (2017).
18. Chen, Y. et al. Cosmic web reconstruction through density ridges: catalogue. *Mon. Not. R. Astron. Soc.* **461**, 3896–3909 (2016).
19. Dawson, K. S. et al. The Baryon Oscillation Spectroscopic Survey of SDSS-III. *Astron. J.* **145**, 10 (2013).
20. Alam, S. et al. The eleventh and twelfth data releases of the Sloan Digital Sky Survey: final data from SDSS-III. *Astron. J. Suppl.* **219**, 12 (2015).
21. Chen, Y., Ho, S., Freeman, P. E., Genovese, C. R. & Wasserman, L. Cosmic web reconstruction through density ridges: method and algorithm. *Mon. Not. R. Astron. Soc.* **454**, 1140–1156 (2015).
22. Planck Collaboration. Planck 2013 results. I. Overview of products and scientific results. *Astron. Astrophys.* **571**, A1 (2014).
23. Planck Collaboration. Planck 2013 results. XVII. Gravitational lensing by large-scale structure. *Astron. Astrophys.* **571**, A17 (2014).
24. Clampitt, J., Jain, B., Takada, M. & Miyatake, H. Detection of stacked filament lensing between SDSS luminous red galaxies. *Mon. Not. R. Astron. Soc.* **457**, 2391–2400 (2016).
25. Epps, S. D. & Hudson, M. J. The weak lensing masses of filaments between luminous red galaxies. *Mon. Not. R. Astron. Soc.* **468**, 2605–2613 (2017).
26. Higuchi, Y., Oguri, M. & Shirasaki, M. Statistical properties of filaments in weak gravitational lensing. *Mon. Not. R. Astron. Soc.* **441**, 745–756 (2014).
27. Planck Collaboration. Planck 2013 results. XVI. Cosmological parameters. *Astron. Astrophys.* **571**, A16 (2014).
28. Limber, D. N. The analysis of counts of the extragalactic nebulae in terms of a fluctuating density field. *Astrophys. J.* **117**, 134 (1953).
29. Rykoff, E. S. et al. redMaPPer I: Algorithm and SDSS DR8 Catalog. *Astron. J.* **785**, 104 (2014).
30. de Graaff, A., Cai, Y. C., Heymans, C. & Peacock, J. A. Missing baryons in the cosmic web revealed by the Sunyaev–Zel'dovich effect. Preprint at https://arxiv.org/abs/1709.10378 (2017).
31. Wassermann, L. *All of Nonparametric Statistics* (Springer Science and Business Media, New York, USA, 2017).
32. Chen, Y. et al. Detecting effects of filaments on galaxy properties in the Sloan Digital Sky Survey III. *Mon. Not. R. Astron. Soc.* **466**, 1880–1893 (2017).
33. Chen, Y. C., Genovese, C. R. & Wasserman, L. Asymptotic theory for density ridges. *Ann. Statistics* **43**, 1896–1928 (2015).
34. Bagla, J. S. A TreePM code for cosmological *N*-body simulations. *Astron. Astrophys.* **23**, 185–196 (2002).

35. White, M. J., Hernquist, L. & Springel, V. Simulating the Sunyaev–Zel'dovich effect(s): Including radiative cooling and energy injection by galactic winds. *Astron. J.* **579**, 16 (2002).
36. Reid, B. A., Seo, H., Leauthaud, A., Tinker, J. L. & White, M. A 2.5 per cent measurement of the growth rate from small-scale redshift space clustering of SDSS-III CMASS galaxies. *Mon. Not. R. Astron. Soc.* **444**, 476–502 (2014).
37. Peacock, J. A. & Smith, R. E. Halo occupation numbers and galaxy bias. *Mon. Not. R. Astron. Soc.* **318**, 1144–1156 (2000).
38. Seljak, U. Analytic model for galaxy and dark matter clustering. *Mon. Not. R. Astron. Soc.* **318**, 203–213 (2000).
39. Benson, A. J., Cole, S., Frenk, C. S., Baugh, C. M. & Lacey, C. G. The nature of galaxy bias and clustering. *Mon. Not. R. Astron. Soc.* **311**, 793–808 (2000).
40. White, M. J., Hernquist, L. & Springel, V. The halo model and numerical simulations. *Astron. J.* **550**, 129–132 (2001).
41. Berlind, A. A. & Weinberg, D. H. The Halo occupation distribution: towards an empirical determination of the relation between galaxies and mass. *Astron. J.* **575**, 587–616 (2002).
42. Cooray, A. & Sheth, R. K. Halo models of large scale structure. *Phys. Rept.* **372**, 1–129 (2002).
43. Beutler, F. et al. The clustering of galaxies in the SDSS-III Baryon Oscillation Spectroscopic Survey: testing gravity with redshift-space distortions using the power spectrum multipoles. *Mon. Not. R. Astron. Soc.* **443**, 1065–1089 (2014).
44. White, M., Tinker, J. L. & McBride, C. K. Mock galaxy catalogues using the quick particle mesh method. *Mon. Not. R. Astron. Soc.* **437**, 2594–2606 (2014).
45. Carlson, J. & White, M. Embedding realistic surveys in simulations through volume remapping. *Astron. J. Suppl.* **190**, 311–314 (2010).

Acknowledgements

We thank A. Pullen and E. Giusarma for discussion, M. White for providing us with the *N*-body simulations, and A. Krolewski and B. Horowitz for comments on the draft. S. Ho is supported by NASA and DOE for this work. S. He is supported by NSF-AST1517593 for this work. S.A. is supported by the European Research Council through the COSFORM Research Grant (#670193). S.F. thanks the Miller Institute for Basic Research in Science at the University of California, Berkeley for support. Some of the results in this paper have been derived using the HEALPix package. The authors would like to acknowledge the support of NERSC.

Author contributions

S. He led the project and most of the manuscript writing. S.A. provided the sky mocks for galaxies and dark matter particles as well as wrote the text relative to sky mock for Filaments and Dark Matter in the Method section. S.F. helped with the theoretical modelling and the interpretation of the results, as well as writing part of the manuscript. Y.C. provided the filament intensity maps for data and simulations. S.Ho conceived the idea of cross-correlating filaments with CMB lensing. All authors contributed to the interpretation of the data and commented on the manuscript.

Competing interests

The authors declare no competing interests.

Additional information

Supplementary information is available for this paper at https://doi.org/10.1038/s41550-018-0426-z.

Reprints and permissions information is available at www.nature.com/reprints.

Correspondence and requests for materials should be addressed to S.H.

Publisher's note: Springer Nature remains neutral with regard to jurisdictional claims in published maps and institutional affiliations.